INTERNATIONAL JOURNAL FOR NUMERICAL AND ANALYTICAL METHODS IN GEOMECHANICS
Int. J. Numer. Anal. Meth. Geomech. 2009; **33**:1407–1423
Published online 23 January 2009 in Wiley InterScience (www.interscience.wiley.com). DOI: 10.1002/nag.771

A mesoscopic model for the behaviour of concrete under high confinement

F. Dupray[1,*,†], Y. Malecot[1], L. Daudeville[1] and E. Buzaud[2]

[1]*Université Joseph Fourier—Grenoble 1, Laboratoire 3S-R, Domaine Universitaire BP53, 38000 Grenoble, France*
[2]*DGA—Centre d'Etudes de Gramat, 46500 Gramat, France*

SUMMARY

When impact loaded, concrete is submitted to high triaxial stresses. The experimental response of concrete under quasi-static triaxial compression is studied using a triaxial press capable of applying a mean pressure greater than 1 GPa on cylindrical samples measuring 7 cm in diameter and 14 cm high. A numerical analysis of these previous experiments is performed herein at a mesoscopic scale. Concrete is modelled as a biphasic material consisting of a mortar (cement paste and fine aggregates) and roughly spherical aggregates (with a diameter exceeding 2 mm) whose characteristics are applied on a regular cubic finite element mesh. A damage-plasticity model is then used to model the behaviour of mortar. An identification of model parameters on mortar samples and the subsequent comparison between numerical and experimental tests will be presented for hydrostatic and triaxial compression. Copyright © 2009 John Wiley & Sons, Ltd.

Received 5 September 2008; Revised 28 November 2008; Accepted 1 December 2008

KEY WORDS: concrete; triaxial compression; mesoscale model; biphasic model; high confinement

1. INTRODUCTION

Concrete is a very common material and as such gets used in many diverse applications ranging from residential construction to bridges, dams or bunkers. This breadth of potential applications is the source of highly varied mixes, differentiated by the cement paste, the type and particle size distribution of aggregates and any eventual additives. The area of research encompassing the present work focuses on the study of problems tied to severe impacts on concrete structures.

Projectiles generate various localized effects including cratering, tunnelling and spalling or shear plugging. Cratering and shear plugging are correlated with the tensile strength of the concrete, i.e. exposure due to multiple reflections in front of the projectile, as explained by Zukas in [1]. The tunnelling phenomenon is tied to dynamic triaxial compression. It is though difficult to impose a

*Correspondence to: F. Dupray, Université Joseph Fourier—Grenoble 1, Laboratoire 3S-R, Domaine Universitaire BP53, 38000 Grenoble, France.
†E-mail: fabrice.dupray@hmg.inpg.fr

controlled load path in dynamic triaxial compression and therefore to characterize the behaviour of concrete under these conditions.

Triaxial compression is the loading type discussed in this paper. Concrete behaviour under such a loading is now relatively well-known, even under very high confinement, via the tests performed on concrete by Gabet *et al.* [2], Schmidt *et al.* [3] and the tests on mortar by Bažant *et al.* [4], Burlion *et al.* [5] and Williams *et al.* [6]. These authors have observed that under the stated conditions, dry concrete reaches what they refer to as a limit state, characterized by the transition from compacting behaviour to dilating behaviour and this occurs either at the peak-level (under low confinement) or during continued axial stress increase (under high confinement).

In 2004, the 3S-R laboratory in conjunction with the *Centre d'Études de Gramat* (CEG, DGA, French Ministry of Defence) launched a research programme on the vulnerability of concrete infrastructures. During a previous stage of this programme, using the same material, Gabet *et al.* studied the influence of loading path on concrete behaviour [7] and Vu examined the influence of both saturation ratio and water–cement ratio [8]. This article presents a mesoscopic model of the experiments conducted by Gabet. The first objective of this mesoscopic model is to better understand the mechanisms controlling concrete behaviour under high confinement by accessing the stress and strain states of the constitutive materials. The second objective consists of building a tool that characterizes the triaxial behaviour of multiple concrete formulations without performing an extensive experimental campaign for each concrete. Uniaxial compression tests are systematically carried out whenever a concrete is used, but it is economically infeasible to carry out as many triaxial tests. For this reason, numerical modelling is intended to complement experimental tests in predicting the triaxial behaviour of various concrete formulations under high confinement.

Variations across concrete formulations can be divided into two basic categories: cement paste variations (water–cement ratio, porosity, fine sand, additives) and aggregate variations (volume, particle size distribution and mechanical characteristics). A numerical concrete must be able to reproduce these variations and their consequences on global behaviour. Our model therefore contains two phases, a mortar (cement paste and fine sand) and inclusions (representing aggregates).

The aim of this article is to present the numerical concrete model, its identification and a comparison with results from the experiments undertaken by Gabet. The first part of the article will discuss the identification of a damage-plasticity model, i.e. the coupled PRM model (see Rouquand *et al.* [9]), on mortar from experimental tests, while the second part will describe the model-building process and offer a comparison of model results with findings obtained experimentally on the concrete.

2. DESCRIPTION OF THE MORTAR BEHAVIOUR

2.1. Composition of the mortar

This study places emphasis on generating a good description of the behaviour of the mortar used within a specific concrete called R30A7, which has undergone extensive high-confinement testing by Gabet and Vu, i.e. up to 650 MPa of confining pressure. The mortar, labelled MR30A7, is composed of the same mixture as the R30A7 concrete, yet without the aggregate category larger than 2 mm in typical size, which in fact represents 40.2% in volume of the R30A7 composition. The specific mortar mixture is given in the table below.

DOI: 10.1002/nag

Element	Proportion in MR30A7 (kg/m^3)	Proportion in R30A7 (kg/m^3)
Silica gravel 2/8	0	1007
Silica sand 0/2 (Silmix)	1464	838
Water	283	169
CEM I 52.5 cement	440	263

2.2. The coupled PRM model

The coupled PRM model is an explicit damage-plasticity model that reproduces the unilateral damage phenomena at low mean stress as well as the nonlinear compaction and plasticity phenomena at high mean stresses, phenomena that have been underlined as the most important by Burlion *et al.* (see [5]). In between the extremes and for high strains, the model combines these two effects. It has been described by Rouquand *et al.* in [9] and is based on both a damage model, i.e. the PRM model (see Rouquand [10] and Pontiroli [11]) and the KST model for plasticity (see Krieg [12] and Swenson and Taylor [13]).

The basis of the PRM model is the Mazars' model [14], a damage model itself based on the theory of damage in continuous media. Mazars' model has only one scalar damage variable and applies the concept of equivalent strain $\tilde{\varepsilon}$ (or equivalent tensile strain, see Equation (3)) in order to determine the damage. Damage is interpreted as a decrease of the useful surface that can be stressed, what leads to the definition of the effective stress $\underline{\underline{\tilde{\sigma}}}=\underline{\underline{\sigma}}/(1-D)$ and its use as in linear elasticity: $\underline{\underline{\tilde{\sigma}}}=\mathbb{\Lambda}\underline{\underline{\varepsilon}}$, where $\mathbb{\Lambda}$ is the fourth-order isotropic stiffness tensor. This concept is easily extended to unilateral damage for which an increase of the useful surface represents the crack closure effect in compression. Figure 1, which shows the response of the model under uniaxial tension and compression, underscores this important feature of the PRM model: damage is unilateral and ensures stiffness recovery in case of compression following damage-inducing tensile loading. Damage is accompanied by inelastic strains in the form of $\varepsilon_{\mathrm{ft}}$. $\varepsilon_{\mathrm{ft}}$ is the focal point of the unloading strains and evolves with the inelastic compressive strains, as can be seen in Figure 1, which represents the response of the model to a tension–unloading–compression–unloading–tension load path. In Mazars' model, the damage evolution law is expressed using parameters not directly identified from usual tests. One of the improvements, which at the same time serves as a limitation, contributed by the PRM model is that the damage law is expressed with typical parameters: f_{c}—compressive strength; f_{t}—tensile strength; E—Young's modulus and ν—Poisson's ratio. The general formulation of the PRM damage model is presented in the following equations:

$$\begin{aligned} \text{under tension } \sigma-\sigma_{\mathrm{ft}} &= E_0(1-D_{\mathrm{t}})(\varepsilon-\varepsilon_{\mathrm{ft}}) \\ \text{under compression } \sigma-\sigma_{\mathrm{ft}} &= E_0(1-D_{\mathrm{c}})(\varepsilon-\varepsilon_{\mathrm{ft}}) \\ \text{general 3D case } \underline{\underline{\sigma}}-\underline{\underline{\sigma}}_{\mathrm{ft}} &= \mathbb{\Lambda}_0(1-D)(\underline{\underline{\varepsilon}}-\underline{\underline{\varepsilon}}_{\mathrm{ft}}) \end{aligned} \tag{1}$$

where E_0 is the initial Young's modulus of the material and $\mathbb{\Lambda}_0$ the fourth-order initial stiffness tensor. D remains a scalar and is calculated from a combination of the two modes of damage

$$D=\alpha_t D_{\mathrm{t}}+(1-\alpha_t)D_{\mathrm{c}} \tag{2}$$

DOI: 10.1002/nag

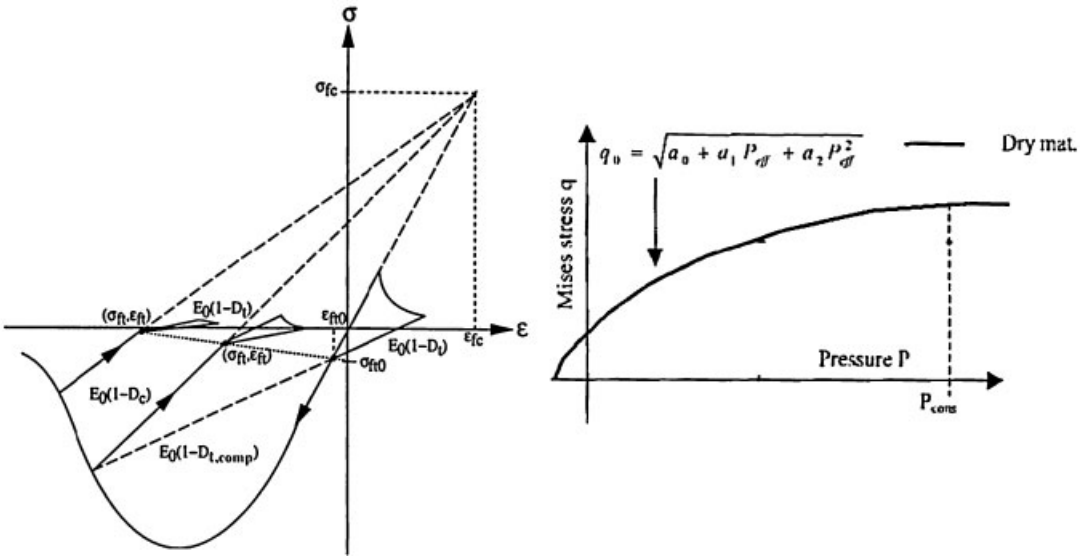

Figure 1. (left): Stress-strain curve of the PRM model for a tensile-compressive loading. $(\varepsilon_{\mathrm{fc}}, \sigma_{\mathrm{fc}})$ is the fixed focal point in compression. $(\varepsilon_{\mathrm{ft}}, \sigma_{\mathrm{ft}})$ is the focal point in tension. D_{t}, D_{c} and $D_{\mathrm{t,comp}}$ are damage variables, respectively, in tension, in compression and the tensile damage due to compressive strains—(right): deviator q vs mean pressure p yield surface in the modified KST model.

where $\alpha_t = f(\underline{\underline{\varepsilon}} - \underline{\underline{\varepsilon}}_{\mathrm{ft}})$ evolves between 0 and 1, and $D_{\mathrm{t\ or\ c}} = f(\tilde{\varepsilon})$ are scalars that characterise the damage due to, respectively, tensile or compressive strains

$$\tilde{\varepsilon} = \sqrt{\sum_i \langle x_i \rangle_+^2} \tag{3}$$

where $\langle x \rangle_+ = x$ if $x > 0$ and $\langle x \rangle_+ = 0$ if not, x_i are the principal strain components in compression and $x_i = (\varepsilon - \varepsilon_{\mathrm{ft}})_i$ in tension.

The KST model is a perfect plasticity model that was enhanced by Rouquand *et al.* in [9] to control the volumetric behaviour (through nonlinear elasticity). It makes use of a piecewise linear curve of the volumetric behaviour to describe the irreversible porosity closure, as seen in Figure 1, along with a parabolic yield surface to describe plastic deviatoric behaviour. The modified KST model is not intended to reproduce dilatancy, therefore, the coupled PRM model is adapted to the modelling of concrete behaviour under its limit state surface and can reproduce the level of stress and strain of the experimental limit state, yet on the other hand cannot reproduce experimentally observed dilatancy. This level of stress is called the limit state for numerical testing.

Coupling between the two models begins with the nonlinear elastic part of the modified KST model, which passes its bulk modulus as an argument to the applied PRM damage law. Damage is inhibited at high mean pressures, even in the presence of previous damage. Not only is there a dependence on strains $\underline{\underline{\varepsilon}}$, but also a strong dependence on the ratio of deviatoric effective stress to mean effective stress $\tilde{q}/\tilde{p}$. It is assumed that the damage is inhibited in a uniaxial strain test and fully developed in a uniaxial compression test. This dependence is included in the model through these equations, where λ_0 and μ_0 are the Lamé coefficients.

DOI: 10.1002/nag

$$D=\alpha_{Dc}(\alpha_t D_t+(1-\alpha_t)D_c) \tag{4}$$

$$\begin{aligned}
&\alpha_{Dc}=0 \quad \text{if } \frac{\tilde{q}}{\tilde{p}}\leqslant\frac{3(1-2\nu)}{1+\nu}\\
&\alpha_{Dc}=1 \quad \text{if } \frac{\tilde{q}}{\tilde{p}}\geqslant 3\\
&\alpha_{Dc}=\frac{(3\lambda_0+2\mu_0)\dfrac{\tilde{q}}{\tilde{p}}-6\mu_0}{9\lambda_0} \quad \text{in between}
\end{aligned} \tag{5}$$

The purpose is to prevent a zone that was damaged under low confinement to appear too soft while subsequently loaded hydrostatically, what would be in contradiction with experimental observations. It also has consequences on the shape of the damage yield surface and the points where it crosses the plastic yield surface. This explicit formulation is not based on thermodynamic principles, but it has the advantage, in comparison with coupled models based on thermodynamics, e.g. the Nguyen and Houlsby model [15] of providing a more accurate description of concrete behaviour in a wide of range of situations.

2.3. Identification of the coupled PRM model parameters for the mortar

In order to perform this identification step, samples of MR30A7 were cast and after hardening dried, then submitted to the following tests: uniaxial compression, three-point-bending, hydrostatic compression and triaxial compression. Uniaxial compression samples were instrumented with two axial gauges and one circumferential gauge, to allow for identification of Young's modulus and Poisson's ratio, in addition to compressive strength. The identified parameters were: $E=25.5\,\text{GPa}$, $\nu=0.16$ et $f_c=59.5\,\text{MPa}$. The comparison between this model and the experimental test is shown in Figure 2. These parameters define the entire shape of the curve and hence do not offer the

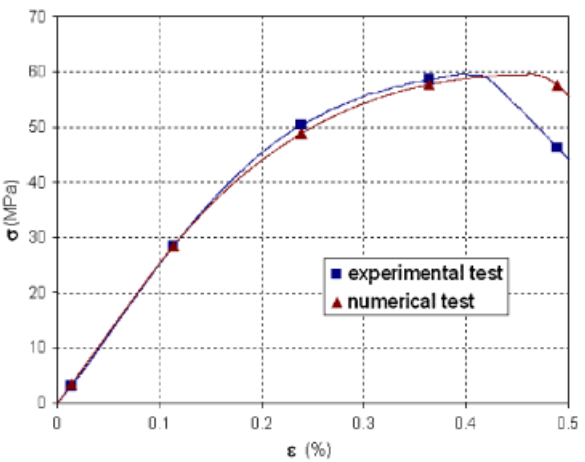

Figure 2. Uniaxial compression test on MR30A7: axial stress σ_1 vs axial strain ε_1—experimental results (■) and identified model (▲).

DOI: 10.1002/nag

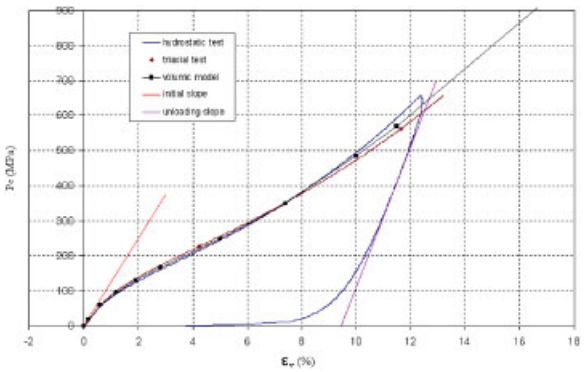

Figure 3. Hydrostatic compression test on MR30A7: confining pressure P_c vs volumetric strains ε_v. View of parameters identified for the modified KST model.

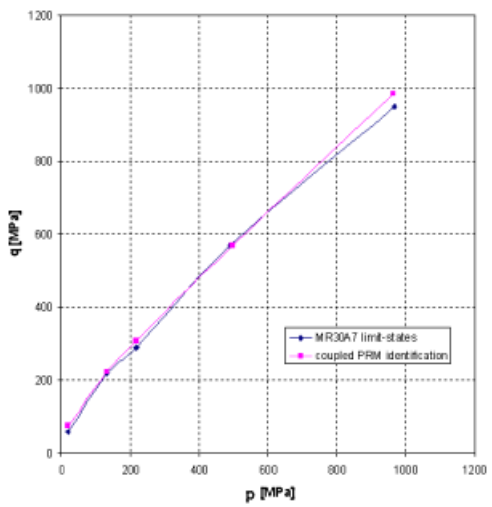

Figure 4. Triaxial compression tests on MR30A7: limit states, defined as transitions from compacting to dilating behaviour for various confining pressures from 0 to 650 MPa, in the q vs p plane.

possibility of adjusting the strain at peak stress to the experimentally derived strain, yet still allow for good agreement with it.

The confined test was performed on the Giga press, a machine operated by 3S-R laboratory in the frame of a collaboration with CEG, this device is able to apply a confining pressure of 650 MPa and an axial force of 13 MN on a large cylindrical sample (7 cm diameter and 14 cm height). The experimental set-up has been thoroughly described by Gabet and Vu in [2]. Various confined tests were performed on mortar samples in order to identify parameters of the modified KST model, including volumetric behaviour, in both loading and unloading (see Figure 3) and deviatoric behaviour (see Figure 4). These tests reveal large deformations and a much greater compaction than that observed on concrete. The results of two triaxial tests (among four performed), at confining

DOI: 10.1002/nag

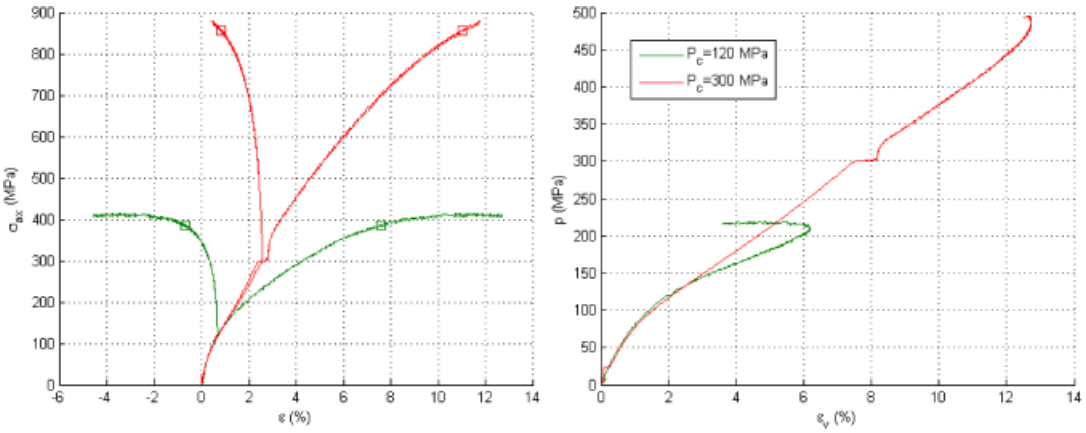

Figure 5. Triaxial compression tests on MR30A7 at 120 and 300 MPa confinement—(left): axial behaviour σ_{ax} vs ε_{ax} (right side) and vs ε_{circ} (left side). The squares represent the limit state as observed on the volumetric curves—(right): volumetric behaviour p vs ε_v.

pressures of 120 and 300 MPa are presented in Figure 5. The dilatancy observed at the limit state on the 120 MPa confinement test is particularly obvious, since the homogeneous character of the mortar authorises measuring large strains even beyond this point. We can observe the same type of curves as on concrete (see Gabet [7]), yet the strains are approximately 45% greater than those recorded on R30A7 concrete specimens in the hydrostatic phase. The initial deviatoric modulus is also greatly reduced, but the triaxial compressive strength under moderate confinement or the limit state under higher confinement exceeds by around 10% than that observed on R30A7.

3. TESTS ON NUMERICAL CONCRETE

3.1. The numerical concrete model

The mesoscale numerical concrete model distinguishes two phases within the concrete: mortar, which includes the cement paste and fine sand (less than 2 mm in size) and aggregates. The two-dimensional approach was first seen and is still used in the area of thermal damage (see for example Menou *et al.* [16]) or with refined approaches (see Pedersen *et al.* [17]). But when applied in three dimensions, this kind of numerical model can only be of very recent use, due to the heavy computational requirements associated with this approach. It has been employed in a number of cases, first by Thoma and Riedel *et al.* (see [18, 19]) for shock response, then for uniaxial compression by Wriggers and Moftah in [20], by Akers and Phillips [21] for contact detonation, and for tension and compression by Caballero *et al.* [22]. Authors give more or less importance to the distribution of aggregates: in Akers' approach, aggregates are cubic and regularly distributed; Riedel's approach however is similar to the one presented herein. The model is a cylinder of the same size as the experimental sample, i.e. 7 cm in diameter and 14 cm high, which is sufficient to ensure the effect of the distribution on the macro-scale behaviour is as limited as possible. The mesh is cubic and regular, which means the cylindrical shape can only be approximated. The aggregates have been modelled as assemblies of elements approximating spheres. The mesh size

DOI: 10.1002/nag

adopted for the tests reported in this article is 2 mm, which leads to a 68 110-element model and means that modelled aggregates may be as small as one element.

The numerical aggregate distribution complies with the size distribution of the actual aggregates in an histogram of six classes. In each class, a random distribution of aggregate centres and diameters is assigned and the potential superposition with previous aggregates is verified. In the absence of superposition, the elements approximating spheres undergo a change in their material properties from mortar to aggregate, until the class is full. The total aggregate fraction in the actual sample is 40.2% and this high percentage is difficult to obtain from such a crude model. It implies the existence of contacts (in this case, bonds) between aggregates. Therefore, this model cannot reproduce relative movements between aggregates, which will be possible with finer meshes. The choice of bonded aggregates and mortar elements is justified in the case of multi-compressive loadings that are considered here. The debonding that is observed experimentally around some aggregates after such a high confinement test is only meaningful in the unloading part of the test, which is not modelled here. The maximal aggregate size is 10 mm. A view of the sample has been given in Figure 6.

The mechanical behaviour of the aggregates is selected to be elastic. The mechanical characteristics of the aggregates were not identified, but instead deduced from their chemical properties: the aggregates are mainly silicates (SiO_2), whose mechanical properties are available in the literature, e.g. in Sellers and Scheele [23]. Young's modulus of silicates is set at $E_{\text{agg},1} = 70\,\text{GPa}$, and Poisson's ratio at $\nu_{\text{agg}} = 0.2$. Simple calculations, such as those performed by Riedel in [19], give the linear elastic parameters of the biphasic model. From this simple comparison in Young's modulus between mortar, aggregates and of actual concrete, it appears that the model would be much too steep in an uniaxial elastic compression, as shown below:

$$\frac{V_{\text{mortar}} E_{\text{mortar}} + V_{\text{aggregates}} E_{\text{aggregates}}}{V_{\text{concrete}}} = 43\,\text{GPa} > E_{\text{concrete}} = 29\,\text{GPa}$$

Figure 6. View of the numerical sample: aggregates are shown in dark grey and mortar in light grey.

DOI: 10.1002/nag

The main reason for this observation is the existence of the interfacial transition zone or ITZ that has very poor mechanical characteristics and high porosity (see [24]). It is possible to integrate its influence in an approximate manner by simultaneously testing numerical concrete with an 'aggregate' Young's modulus set at $E_{\mathrm{agg},2} = 35$ GPa, which gives the numerical concrete the correct Young's modulus of 29 GPa and takes into account the presence of the ITZ in the 'aggregate' phase of numerical concrete.

3.2. *Hydrostatic behaviour*

The hydrostatic behaviour of the numerical concrete has been assessed by means of comparison with the actual concrete tested by Gabet (see [7]). Gabet's tests were performed on dry concrete and the investigated concrete is a mixture of the test mortar and quartzite aggregates. Our model does not take into account the interactions occurring between the two phases, since they are considered to be bonded. As can be seen in Figure 7, it appears that the differences between the mortar and the concrete are well replicated, with a very significant decrease in total volumetric strain, yet the numerical concrete remains too steep, even with the reduced Young's modulus of the aggregate. It should be noted that the discrepancy observed between the experimental and numerical curves (with $E_{\mathrm{agg},2}$) is concentrated between 50 and 300 MPa. The initial slopes are close and in the range above 300 MPa, the strain difference remains nearly constant at 1%. The interpretation of this phenomenon is that some physical pore collapse, happening in this range of pressures, is not reproduced in the model and this may again be the collapse of the high-porosity ITZ. A control of an eventual gap in porosity between the mortar cast alone, non-vibrated or cast with aggregates and vibrated, could also be a source of discrepancy. A key observation can be drawn however from Figure 8, mean pressure p in the mortar is much lower than in aggregates. At a global mean pressure of 650 MPa, average mean pressure in the mortar only amounts to 460 MPa, while it equals 919 MPa in the aggregates. This phenomenon is encountered from the start of the hydrostatic compression and is significant beginning from 50 MPa confinement, as can be seen in the right part of Figure 8.

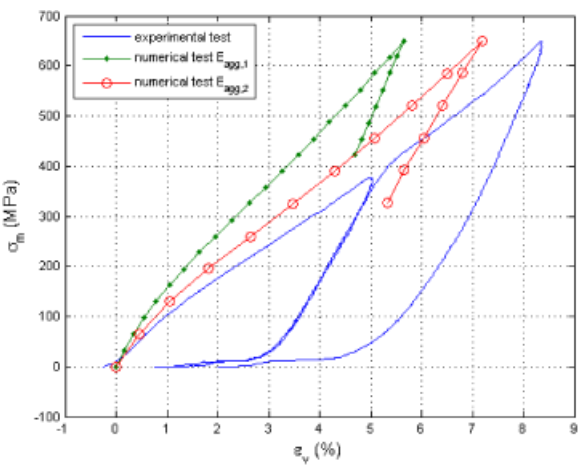

Figure 7. Hydrostatic compression tests on actual and numerical concrete: comparison of volumetric behaviour σ_{m} vs ε_{v}.

DOI: 10.1002/nag

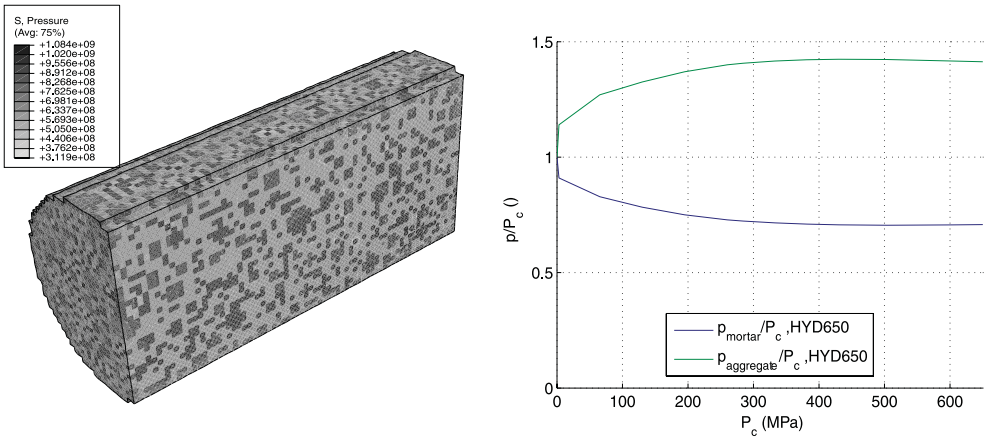

Figure 8. Hydrostatic compression test on numerical concrete: (left) map of the pressures in a cut of the sample with $E_{\mathrm{agg},2}$—(right) evolution of the pressure ratios in mortar and aggregates.

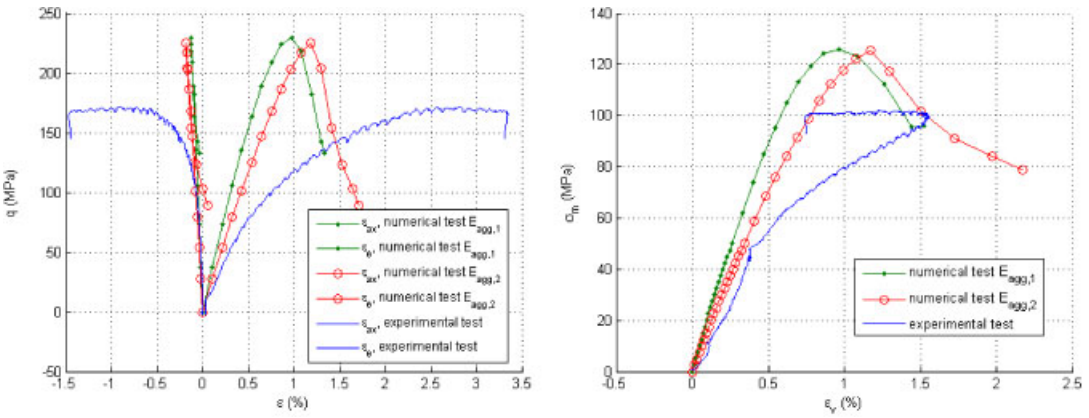

Figure 9. Triaxial compression tests at $P_{\mathrm{c}} = 50\,\mathrm{MPa}$ on actual and numerical concrete—(left): comparison in deviatoric behaviour q vs ε—(right): comparison in volumetric behaviour σ_{m} vs ε_{v}.

3.3. Triaxial behaviour

In order to have a global view of the capability of the numerical concrete model to describe concrete behaviour under triaxial compression, the tests implemented will be oriented around three aspects: axial behaviour, volumetric behaviour and the limit states, and cracking pattern. Three levels of confinement are compared with the equivalent experimental tests: 50, 200 and 650 MPa.

3.3.1. Axial behaviour. Since the hydrostatic behaviour of the model has already been presented, this section will focus on the deviatoric behaviour, i.e. the von Mises stress q compared with the axial and circumferential strains $\varepsilon_{\mathrm{ax}}$ and $\varepsilon_{\mathrm{circ}}$. Under moderate confinement ($P_{\mathrm{c}} = 50\,\mathrm{MPa}$), results are shown in Figure 9 and the tangent modulus of the actual concrete decreases gradually, as of the

DOI: 10.1002/nag

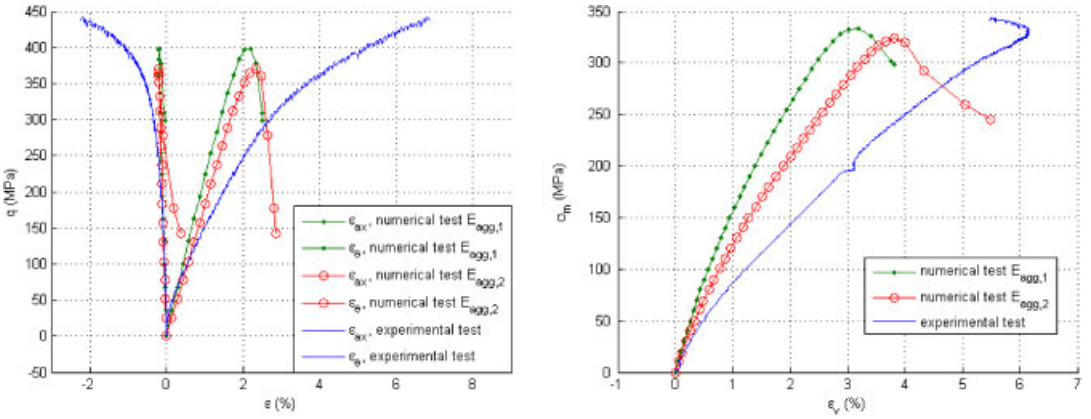

Figure 10. Triaxial compression tests at $P_c = 200$ MPa on actual and numerical concrete—(left): comparison in deviatoric behaviour q vs ε—(right): comparison in volumetric behaviour σ_m vs ε_v.

start of the triaxial loading. This behaviour has not been reproduced in our model, wherein damage occurs at a higher stress level and less progressively. The moduli therefore are only comparable at the beginning of the loading, and preferably with the $E_{agg,2}$ concrete. The difference in moduli between the two numerical concrete formulations is comparable to that observed hydrostatically, which would indicate that they are both working as a composite. The comparison between the experimental and numerical circumferential behaviours leads to better results. It is also worth noting that both specimens exhibit a softening behaviour.

Under higher confinement ($P_c = 200$ MPa), Figure 10 shows more similarities between the numerical and experimental concrete. The tangent modulus of the numerical concrete with $E_{agg,2}$ is close to that of the actual concrete up until half the loading, yet the same observations as in the 50 MPa case can still be made here. The initial very high slope of the experimental test is correlated with the creep occurring between the end of the hydrostatic phase and the beginning of the triaxial loading. It is clear that the numerical deviatoric behaviour is not linear, which means that the numerical concrete with the coupled PRM model, is able to reproduce damage behaviour at this level, this would not be possible with the coupled PRM model when used in a monophasic sample (see Gabet's Ph.D. dissertation p. 149 [25]). This phenomenon is easily explained by the presence of aggregates, which causes stress concentrations in between aggregates, in a mortar where the mean pressure remains quite low (160 MPa). It should also be noted that the difference in modulus between the two numerical concrete formulations is much smaller than when under moderate confinement.

The results from tests conducted under very high confinement ($P_c = 650$ MPa) are presented in Figure 11 and show a better correlation between numerical and experimental behaviour, as the damaging behaviour of the actual concrete is less obvious under high pressure, since mortar damage process has already been completed by the hydrostatic pressure. The difference between the two numerical concrete formulations is once again reduced in comparison with the lower confinement tests.

3.3.2. Volumetric behaviour and limit states. Results are presented on the right-hand side of Figures 9–11. In addition to what has already been discussed regarding the hydrostatic phase, it

DOI: 10.1002/nag

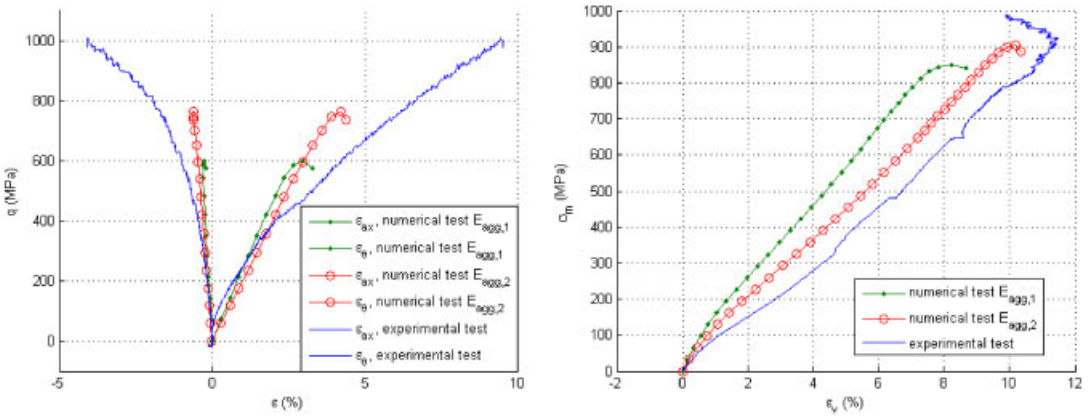

Figure 11. Triaxial compression tests at $P_c = 650$ MPa on actual and numerical concrete—(left): comparison in deviatoric behaviour q vs ε—(right): comparison in volumetric behaviour σ_m vs ε_v.

appears that the volumetric behaviour of numerical concrete in the triaxial phase fits the experimental behaviour better with increasing confining pressure.

For the 50 MPa confinement test, the experimental volumetric behaviour is considerably away from the hydrostatic curve, whereas the numerical curve lies close to this behaviour. The peak-stress level is comparable but softening is more pronounced than expected. Results are much better at 200 MPa, since the volumetric behaviour shows greater similarity and the stress level of the actual limit state is accurately described by the peak stress of the numerical model, as was initially intended. But again softening appears instead of the observed dilatancy. At this level, the influence of aggregate modulus on the limit state remains limited. At 650 MPa, the volumetric curves of the numerical tests in the triaxial phase are very similar to the experimental curve. Moreover, the limit state is the same as the experimentally derived limit state.

3.3.3. Cracking patterns. The ability of the model to predict the shape of fractured samples is evaluated in Figures 12–14. At 50 MPa, the numerical sample exhibits two damage zones, a larger zone near one end of the sample and a smaller zone near the other. These zones are not perpendicular to the sample axis and become clearly visible just after the peak. Though the slope observed in the actual sample is greater than that in the numerical model, the similarities are nonetheless remarkable.

At 200 MPa, the model is able to replicate damage localization, as presented in Figure 13, in comparison with a photograph of the actual sample. The numerical sample exhibits two symmetrical damage zones, both perpendicular to the sample axis. This localization is visible before the peak, though Figure 13 shows the sample precisely at peak stress. This is exactly what can be observed on the photograph of the actual sample.

At 650 MPa, the numerical model exhibits insufficient damage in comparison with the actual sample. Damage only appears after the peak, when large plastic strains enable it. The ratio $\tilde{q}/\tilde{p}$ rarely exceeds $3(1-2\nu)/(1+\nu) = 1.75$, resulting in almost no damage. Sample axial stress is indeed affected by local plasticisation, detected by a slight increase in mortar maximal compressive principal strains, the map of which is presented in Figure 14. Although not very clear in the

DOI: 10.1002/nag

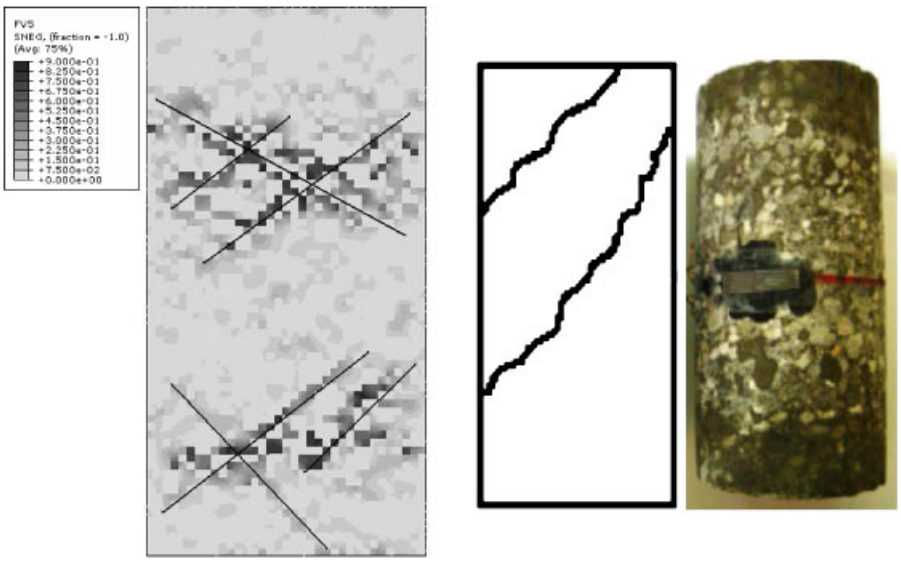

Figure 12. Triaxial compression test at $P_c = 50\,\text{MPa}$ on numerical concrete: map of the damage in a cut of the sample with $E_{agg,2}$, compared to a scheme and a photograph of an actual sample.

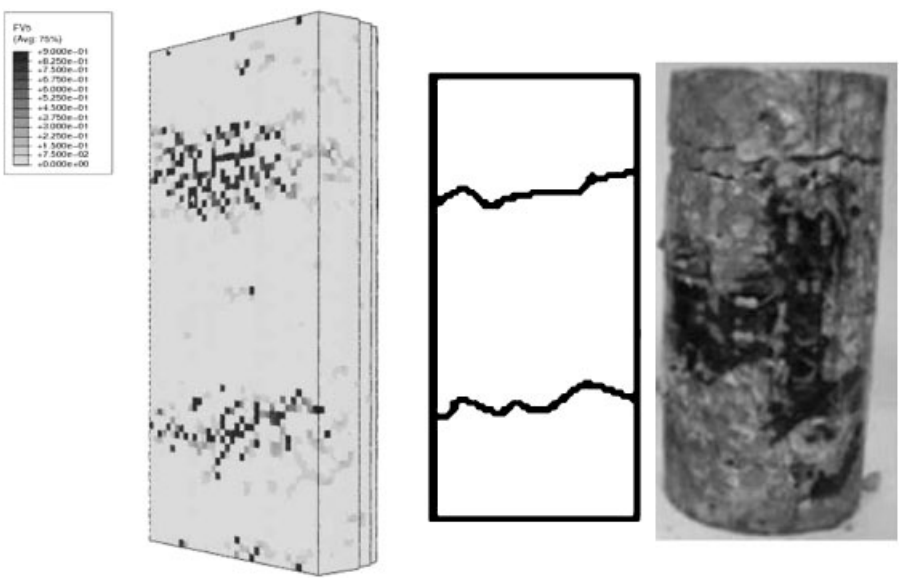

Figure 13. Triaxial compression test at $P_c = 200\,\text{MPa}$ on numerical concrete: map of the damage in a cut of the sample with $E_{agg,2}$, compared to a scheme and a photograph of an actual sample.

DOI: 10.1002/nag

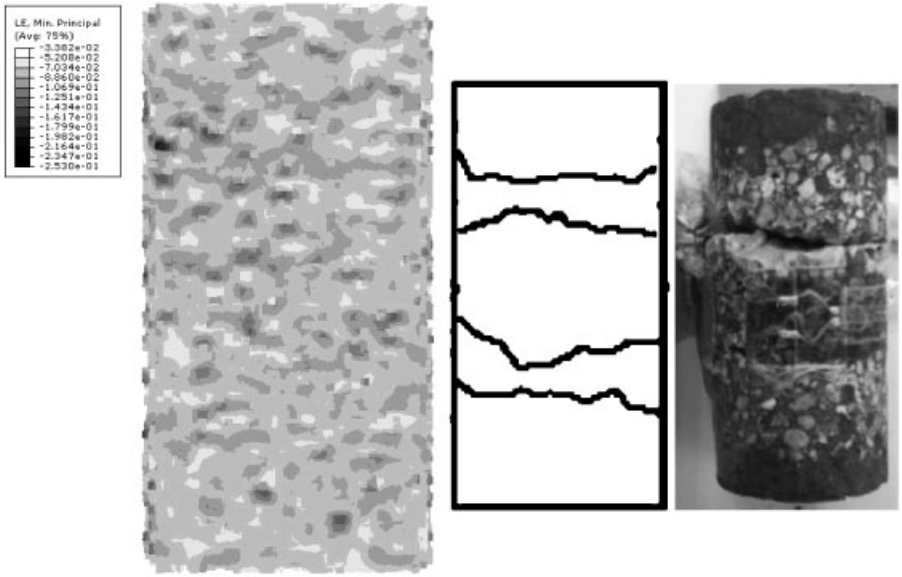

Figure 14. Triaxial compression test at $P_c = 650$ MPa on numerical concrete: map of the maximal principal compressive strains (only the mortar elements are represented) in a cut of the sample with $E_{agg,2}$, compared to a scheme and a photograph of an actual sample.

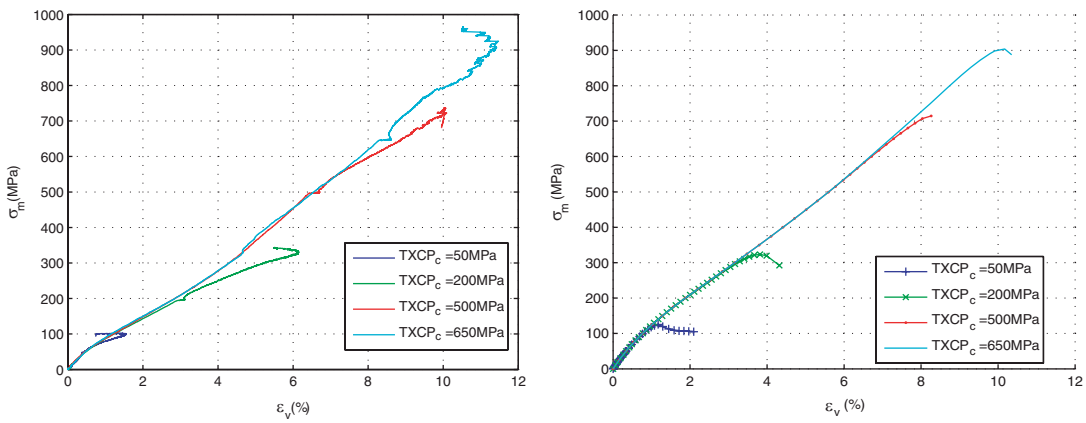

Figure 15. Volumetric behaviour of the experimental (left) and numerical (right) tests: σ_m vs ε_v.

figure and very affected by the presence of aggregates, the orientation of the phenomena is rather perpendicular to the axis, just as in the actual sample.

When various tests are performed with slightly varying parameters or a different aggregate distribution, the observed cracking patterns are also varying but keep the same characteristics: typically the cracking bands are more or less close to the middle of the specimen or a third horizontal band can appear at 200 MPa. These variations are common on the experimental samples too.

DOI: 10.1002/nag

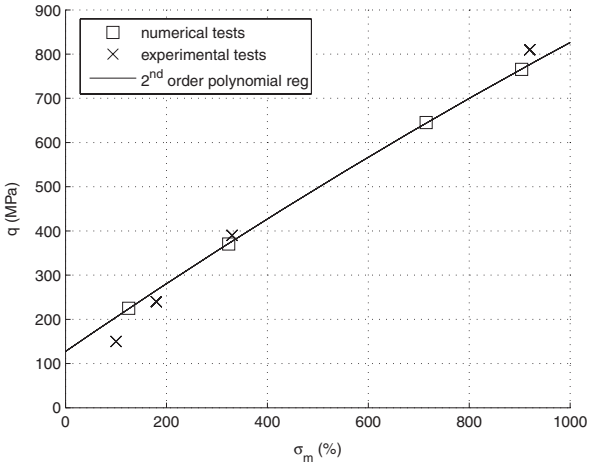

Figure 16. Limit states of numerical and actual concrete in the q vs $p = \sigma_m$ plane—second order polynomial regression of the numerical limit states.

3.3.4. Global results of the triaxial tests. The main results of this study have been compiled in Figure 15. A comparison with experimental results highlights two facts. First, and in contrast with the monophasic model, deviatoric behaviour does not follow the hydrostatic volumetric curve. Just as with actual concrete, it is more contracting under triaxial loading than under hydrostatic loading. Second, the limit states for the various confining pressures tested are compared with experiments in Figure 16. It would appear that above 100 MPa, the numerical model provides an accurate limit state surface.

4. CONCLUSION

Although the numerical model used herein is a very simplified view of the mesoscale mechanics in concrete, it already provides a reproduction of the main characteristics of concrete behaviour under high confinement, both qualitatively and quantitatively: mortar compaction, damage localization, aggregate influence on the limit state with respect to mortar and load path influence on volumetric behaviour. The fact that it correctly reproduces the damage zones observed on actual samples suggests that this model can help in the understanding of mesoscale phenomena and their influence on macroscale behaviour. It clearly appears that the simple presence of aggregates induces a sizable difference with mortar behaviour, not only in terms of rigidity, but throughout the hydrostatic phase and in the second half of the deviatoric curve. During the hydrostatic phase, the presence of aggregates causes a major decrease in mean pressure of the concrete mortar phase in comparison with the mortar alone. The consequence of this finding is that the deviatoric behaviour of concrete at a given confinement does not depend on the deviatoric strength of the mortar at the same confinement, but instead at a significantly lower confinement. Further numerical tests are being performed in order to include some well-known facts about the mesoscale mechanics of concrete, including the presence of an interfacial transition zone (ITZ), and differences in mortar

DOI: 10.1002/nag

characteristics when cast either alone or with aggregates (greater porosity and all the ensuing consequences).

REFERENCES

1. Zukas JA. *Impact Dynamics*. Krieger: Malabar, FL, U.S.A., 1992.
2. Gabet T, Hong Vu X, Malécot Y, Daudeville L. A new experimental technique for the analysis of concrete under high triaxial loading. *Journal de Physique IV* 2006; **134**:635–640.
3. Schmidt MJ, Cazacu O, Green ML. Experimental and theoretical investigation of the high-pressure behavior of concrete. *International Journal for Numerical and Analytical Methods in Geomechanics* 2008; DOI: 10.1002/nag.700.
4. Bažant ZP, Bishop FC, Chang TP. Confined compression tests of cement paste and concrete up to 300 ksi. *ACI Journal* 1986; **33**:553–560.
5. Burlion N, Pijaudier-Cabot G, Dahan N. Experimental analysis of compaction of concrete and mortar. *International Journal for Numerical and Analytical Methods in Geomechanics* 2001; **25**:1467–1486.
6. Williams EM, Akers SA, Reed PA. Laboratory characterization of fine aggregate cementitious material. *Technical Report ERDC/GSL TR-05-16*, US Army Engineer Research and Development Center, July 2005.
7. Gabet T, Malécot Y, Daudeville L. Triaxial behaviour of concrete under high stresses: influence of the loading path on compaction and limit states. *Cement and Concrete Research* 2008; **38**(3):403–412.
8. Hong Vu X. Caractérisation expérimentale du béton sous fort confinement: influence du degré de saturation et du rapport eau/ciment. *Thèse de doctorat*, Laboratoire 3S-R, 2007.
9. Rouquand A, Pontiroli C, Mazars J. Concrete structures under severe loading: a strategy to model the response for a large range of dynamic loads. *Fracture Mechanics of Concrete and Concrete Structures*: *Proceedings of FraMCoS-6*, Catania, Italy, 2007.
10. Rouquand A. An explicit damage model for dynamic concrete behaviour. Numerical simulations and comparisons with experimental results on reinforced concrete plates under blast loading. *International Conference on Structures Under Shock and Impact*, Udine, Italy, 1996. DOI: 10.2495/SUSI960301.
11. Pontiroli C. Comportement au souffle de sturctures en béton armé, analyse expérimentale et modélisation. *Thèse de doctorat*, ENS Cachan, CEG, 1995.
12. Krieg RD. A simple constitutive description for soils and crushable foams. *Technical Report SC-DR-72-0883*, Sandia National Laboratories, Albuquerque, 1972.
13. Swenson DV, Taylor LM. A finite element model for the analysis of tailored pulse simulation of boreholes. *International Journal for Numerical and Analytical Methods in Geomechanics* 1983; **7**(4):469–484.
14. Mazars J. A description of micro- and macroscale damage of concrete structures. *Engineering Fracture Mechanics* 1986; **25**(5–6):729–737.
15. Nguyen GD, Houlsby GT. A coupled damage-plasticity model for concrete based on thermodynamic principles: part II: non-local regularization and numerical implementation. *International Journal for Numerical and Analytical Methods in Geomechanics* 2008; **32**(4):391–413.
16. Menou A, Mounajed G, Boussa H, La Borderie C, Lefdi K. Thermal damage approach of concrete: application to specimens subjected to combined compressive and high temperature loads. *High Temperature Materials and Processes* 2008; **27**(1):23–39.
17. Pedersen RR, Simone A, Sluys LJ. Multiple-scale analysis of impact fracture. In *IX International Conference on Computational Plasticity*, Owen DRJ, Oñate E, Suárez B (eds). Barcelona, Spain, 2007.
18. Thoma K, Riedel W, Hiermaier S. Mesomechanical modeling of concrete shock response experiments and linking to macromechanics by numerical analysis. *Proceedings of European Conference on Computational Mechanics*, München, Germany, 1999.
19. Riedel W, Wicklein M, Thoma K. Shock properties of conventional and high strength concrete: experimental and mesomechanical analysis. *International Journal of Impact Engineering* 2008; **35**:155–171.
20. Wriggers P, Moftah SO. Mesoscale models for concrete: homogenisation and damage behaviour. *Finite Elements in Analysis and Design* 2006; **42**(7):623–636.
21. Akers SA, Bruce Phillips R. Concrete modeled as an inhomogeneous material: numerical simulations of contact detonations charges. *18th International Symposium on Military Aspects of Blast and Shock*, Bad Reichenhall, Germany, 2004.
22. Caballero A, Carol I, López CM. A meso-level approach to the 3d numerical analysis of cracking and fracture of concrete materials. *Fatigue and Fracture of Engineering Materials and Structures* 2006; **29**(12):979–991.

23. Sellers E, Scheele F. Prediction of anisotropic damage in experiments simulating mining in witwatersrand quartzite blocks. *International Journal of Rock Mechanics and Mining Sciences and Geomechanics Abstracts* 1996; **33**(7):659–670.
24. Scrivener KL, Nemati KM. The percolation of pore space in the cement paste/aggregate interfacial zone of concrete. *Cement and Concrete Research* 1996; **26**(1):35–40.
25. Gabet T. Comportement triaxial du béton sous fortes contraintes: influence du trajet de chargement. *Thèse de doctorat*, Laboratoire 3S-R, 2006.

DOI: 10.1002/nag